Journal of Colloid and Interface Science 686 (2025) 1188–1199

Contents lists available at ScienceDirect

Journal of Colloid And Interface Science

journal homepage: www.elsevier.com/locate/jcis

Regular Article

Enhanced CO_2 electrochemical reduction on single-atom catalysts with optimized environmental, central and axial chemical ambient

Zhongze Bai [a], Xi Zhuo Jiang [b,*], Kai H. Luo [a,*]

[a] Department of Mechanical Engineering, University College London, Torrington Place, London WC1E 7JE UK
[b] School of Mechanical Engineering and Automation, Northeastern University, Shenyang, Liaoning 110819, PR China

GRAPHICAL ABSTRACT

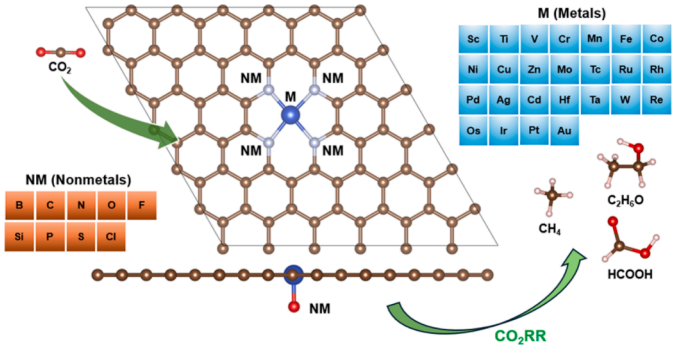

ARTICLE INFO

Keywords:
Single atom catalysts
AIMD
Electrocatalytic CO_2 reduction
Density functional theory
Coordination sphere

ABSTRACT

Single-atom catalysts (SACs) have received significant research interests for electrocatalytic CO_2 reduction reaction (CO_2RR) to produce valuable chemicals. Designing optimal SACs for CO_2RR is a great challenge because of the strong scaling relationship among the many carbon-containing intermediates. In this study, we designed high-performance SACs, breaking the scaling relationship through changing environmental nonmetals, central atoms and axial nonmetals together via a series of density functional theory (DFT) calculations. After screening through configuration stabilities, CO and CO_2 adsorption energy, limiting potential of H_2, product adsorption energy, limiting potential of products, energy barrier of C–C coupling process and AIMD simulations, we finally observed ten optimal SACs (Ti-N4-B, Ti-N4-Si, Ti-CN3-Si, Ti-CN2O(1)-S, Sc-C2NO(1)-B, Sc-C2NO(1)-Si, Ti-BCN2(2)-N, Sc-CN2O(3)-Si, Ru-C2NO(3)-C and Ti-BONC-C) after considering 4311 possible configurations with high activity and selectivity for HCOOH, CH_4 and C_2H_6O formation. Among them, Ti-N4-B, Ru-C2NO(3)-C, and Sc-C2NO(1)-B have the lowest overpotentials for producing HCOOH, CH_4, and C_2H_6O with U_L of −0.2 V, −0.29 V, and −0.51 V, respectively. Subsequently, electronic analysis is implemented to provide a more comprehensive explanation at the electronic level for the enhanced CO_2RR performance of the discovered SACs. Our research demonstrates that the performance of SACs on CO_2RR can be significantly enhanced and altered by the combination of environmental nonmetals, central atoms, and axial nonmetals in a rational design. Importantly, it also establishes a design principle for the rapid screening of prospective catalysts for CO_2RR with high activity and selectivity.

* Corresponding authors.
E-mail addresses: jiangxz@mail.neu.edu.cn (X.Z. Jiang), k.luo@ucl.ac.uk (K.H. Luo).

https://doi.org/10.1016/j.jcis.2025.02.015
Received 7 January 2025; Received in revised form 1 February 2025; Accepted 3 February 2025
Available online 4 February 2025

1. Introduction

Carbon dioxide (CO_2) emissions from fossil fuel combustion and industry contribute significantly to the greenhouse effect [1–3]. Electrocatalytic conversion of CO_2 to chemicals through renewable power is a promising and effective approach for lowering CO_2 concentrations in the atmosphere, alleviating global warming and the energy crisis [4,5]. Currently, the electrocatalytic process for CO_2 reduction reaction (CO_2RR) faces many challenges in such as the unsatisfactory products selectivity, high overpotential and sluggish kinetics of C_2 products [6–8]. Therefore, the development of highly selective and efficient electrocatalysts for the CO_2RR is of great importance and necessary.

In recent years, MNC single-atom catalysts (SACs), which consist of a central metal coordinated with four nitrogen (N) atoms supported on carbon material, have received significant research interests because of their high catalytic activity, maximum atom utilisation, well-turned active sites and tunable electronic properties [9,10]. Among the many metallic elements, copper (Cu) is commonly considered the promising electrocatalyst for CO_2RR because of its great abilities to generate highly attractive multi-electron reduction products [11]. Bai and co-workers systemically studied the CO_2RR performance of Cu-based SACs with different configurations named CuNC-3-pyridine, CuNC-4-pyridine, CuNC-3-pyrrole and CuNC-4-pyrrole through density functional theory (DFT) calculations [12]. They found that CuNC-4-pyridine had outstanding thermodynamic as well as kinetic stabilities and the C–C coupling process during CO_2RR was exothermic, which could greatly facilitate the generation of more desirable C_2 products due to their higher energy storage density and commercial value. However, there are still challenges for CuNC-4-pyridine, for instance, high CO_2 and CO adsorption energies inhibiting CO_2 activation and further catalytic conversion of CO to the multi-electron reduction products, high overpotentials for products generation, etc. As a result, we need to further improve the CO_2RR behaviours for SACs through rational configuration design.

Tuning environmental non-metal atoms, regulating central metal atoms and constructing axial chemical environments are considered highly effective strategies to optimize the catalytic performance of SACs during CO_2RR [11,13]. For instance, Yang and co-workers carried out DFT simulations to study the catalytic activity of Fe, Co, and Ni on nitrogen-doped graphene for CO_2RR [14]. The results show that central metal atoms present a significant effect on reduction paths, overpotential and preferred products during CO_2RR. Wang and co-workers designed Bi-N3S configuration and proved the addition of S may significantly reduce the Gibbs free energy by 0.38 eV for the *COOH formation compared to the Bi-N4 configuration, facilitating the CO_2RR catalytic process [15]. Ni-N_3B SAC was explored by Fu and co-workers via DFT calculations that showed high efficiency and selectivity for the production of CH_4; however, Ni-N_4 was favourable for the CO generation [16]. Li and co-workers found that the introduction of the P atom in Fe-N4 generating Fe-N3P configuration could greatly promote the formation of CO [17]. Chen and co-workers examined 1060 possible SACs, comprising combinations of 20 transition metal atoms and 53 distinct nonmetal bonded environments, using a high-throughput computational screening approach and effectively presented 94 viable SACs for CO_2RR [18]. Huang and co-workers successfully synthesised Ni-N4-O configuration with an O atom of axial coordination and demonstrated Ni-N4-O could transfer CO_2 to CO with high Faradaic efficiency (maximum of 97.2 %) and high stability [19]. Wang et al. conducted a thorough investigation of the function of axial O coordination in the M-N4 structure, finding some exceptional and promising SACs like Os-N4O, Ru-N4O, and Rh-N4O [20]. Peng and co-workers designed the Ni-N4-Cl configuration and found the axially coordinated Cl atom could greatly promote COOH intermediate generation on single-atom Ni sites and therefore enhance the CO_2RR process [21]. While significant progress has been made in SACs for CO_2RR, most studies focus on C_1 products, lacking a systematic analysis of C_2 products distribution. Given their higher energy density and industrial value, understanding C_2 products formation is crucial for optimizing catalytic selectivity and improving CO_2 conversion efficiency. A deeper insight into C_2 products distribution can guide the design of more efficient electrocatalysts, advancing selective CO_2 conversion technologies for sustainable energy and high-value chemical production. Besides, the chosen adsorption site of intermediates for those investigations is only the metal atom, ignoring the function of surrounding atoms, which may result in an unsatisfactory assessment of catalyst capabilities. At last, could the combination of the three methods mentioned above lead to the design of novel and outstanding catalysts for CO_2RR with high activity and selectivity?

To overcome the aforementioned challenges, in this study, we carried out intensive DFT calculations to explore high-performance SACs by tuning environmental non-metal atoms, central metal atoms and constructing axial chemical environments for the generation of both C_1 and C_2 products including HCOOH, CH_3OH, CH_4, C_2H_6O, C_2H_4 and C_2H_6 during CO_2RR. We considered 25 transition elements (Sc, Ti, V, Cr, Mn, Fe, Co, Ni, Cu, Zn, Mo, Tc, Ru, Rh, Pd, Ag, Cd, Hf, Ta, W, Re, Os, Ir, Pt and Au) for central atoms and 9 nonmetals (B, C, N, O, F, Si, P, S and Cl) for environmental and axial atoms. The detailed SACs design and selection processes are presented in Section 2.2.

2. Methods

2.1. DFT calculations

All spin-polarized DFT simulations were performed using the Vienna Ab initio Simulation Package (VASP) package [22,23]. The revised Perdew-Bruke-Ernzerh (RPBE) with the generalised gradient approximation (GGA) was adopted to describe the exchange–correlation interactions [24]. The core electrons were handled using the projector augmented-wave (PAW) approach [25]. Van der Waals interactions between atoms were considered using the DFT-D3 approach with the Becke-Johnson damping [26,27]. The solvent influence was taken into consideration by the VASPsol implicit solvent model with ∈r of 78.4 [28–31]. The cutoff energy and Monkhorst-Pack k-point grids were set for 500 eV and 3 × 3 × 1, respectively. A 20 Å vacuum was introduced along the Z axis to avoid interactions between different layers in periodic boundary conditions. The Hellmann-Feynman force and electronic energy convergence criteria were set to 0.02 eV/Å and 1.0×10^{-5} eV, respectively. The CHE model was used to compute the Gibbs free energy (ΔG) of intermediates during CO_2RR [32,33]. To compute reaction barriers, the transition state (TS) was calculated through the climbing image nudged elastic band (CI-NEB) method [34]. Furthermore, VASPKIT [35] and QVASP [36] programs were utilised to help with the DFT calculations. Local Orbital Basis Suite Towards Electronic-Structure Reconstruction (LOBSTER) was used for Crystal orbital Hamilton population (COHP) computations [37]. All ab initio molecular dynamics (AIMD) computations were carried out through Nose-Hoover thermostat ensemble for 10 ps with a timestep of 0.5 fs. The data for the Cu-N4 structure come from our earlier study [12].

The adsorption energy (E_{ads}) of intermediates was calculated by the following formula:

$$E_{ads} = E_{M/C} - E_C - E_M \quad (1)$$

where $E_{M/C}$, E_C, and E_M represent the total energy of catalyst and adsorbates, the energy of catalyst and the energy of adsorbates, respectively.

The Gibbs free energy (ΔG) change for varying species was calculated with the following equation [38]:

$$\Delta G = \Delta E + \Delta E_{ZPE} - T\Delta S \quad (2)$$

where the difference in electron energies, ΔE, is calculated directly from DFT calculations. ΔE_{ZPE} and ΔS represent the difference in zero-point

energy and entropy between 0 K and room temperature of 298.15 K, respectively.

The limiting potential (U_L) was obtained by Equation (3) [39–41]:

$$U_L = -\Delta G_{max}/e \quad (3)$$

where ΔG_{max} is the free energy change between the potential limiting step (PLS) in CO_2RR at 0 V and the reversible hydrogen electrode (RHE).

Formation energy (E_f) was calculated as stated in Equation (4) to assess the thermodynamic stability of catalysts.

$$\Delta E_f = E_{Catalyst} + a\mu_C - (E_{gra} + \sum \mu_{nonmetal} + \mu_{metal}) \quad (4)$$

where $E_{Catalyst}$ and E_{gra} were the total energies of optimised catalysts and pure graphene with 72 atoms, respectively. The energies of the nonmetal atom ($\mu_{nonmetal}$) and single carbon atom (μ_C) were estimated using stable monomers of the element. μ_{metal} is the energy of single metal atom in vacuum. The variable a represented the number of C atoms that varied between catalysts and pure graphene.

The binding energy (E_{bin}) and cohesive energy (E_{coh}) are adopted to estimate the binding performance between graphene substrate and metal atoms, which was calculated by the following formula [42]:

$$E_{bin} = (E_{M/C} - E_{sub} - \mu_{metal})/n \quad (5)$$

$$E_{coh} = E_{bulk} - m\mu \quad (6)$$

where n and m represented the number of metal atoms in catalysts and bulk metals, respectively. The term μ refers to the energy of a single metal atom in relation to the bulk metal.

Gibbs free energy barrier (G_b) was calculated as the following formula:

$$G_b = G(TS) - G(IS) \quad (7)$$

where G(TS) and G(IS) represented the energies of transition state and initial state, respectively.

2.2. SACs design and screening process

As shown in Fig. 1a, the structure of the designed SACs consists of three parts: environmental nonmetals (NM), central metals (M) and axial nonmetals (NM). Considering the huge consumption of time and computational resources for DFT computation, we sequentially designed the environmental, central and axial environments based on the Cu-N4 configuration. Specifically, we first changed the environmental NM based on the Cu-N4 structure, then filtered out the stable structures. After that, based on the stable configurations obtained above, we designed their central M and selected the stable structures. Finally, we added axial NM for the above stable catalysts and chose stable configurations for further investigation. The criterion for stable structures is the values of formation energies E_f as well as the difference between the binding and cohesive energies E_{b-c} ($E_{b-c} = E_{bin} - E_{coh}$) are negative, which indicates catalysts are thermodynamically stable and central metals prefer to spread atomically across graphene rather than aggregate into nanoparticles because of the coordination effect [9,12].

Due to the symmetry of SACs, we rationally design the

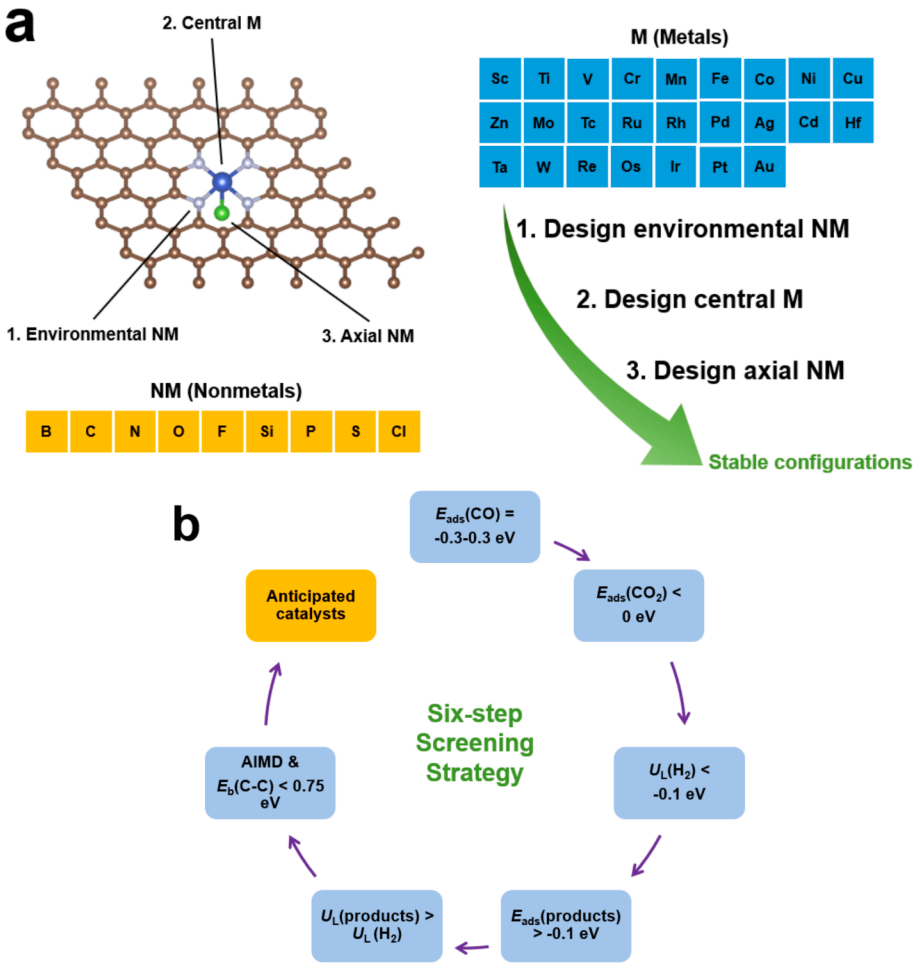

Fig. 1. (a) Construction of stable configurations for SACs and corresponding M and NM elements. (b) A six-step screening strategy to obtain the optimal CO_2RR catalysts.

environmental structures to avoid the duplication of calculations. As shown in Fig. S1, there are five types of environmental structures including A4, A3B, A2B2, ABC2 and ABCD. Here, A, B, C and D represent four different non-metal elements from nine non-metal atoms (B, C, N, O, F, Si, P, S, Cl). A4 represents four identical NM in the coordination environment with a total of nine possible structures. A3B indicates two different elements in the ambient non-metallic atoms, where one element has three atoms and the other one has one atom, giving a total of 72 possible structures. A2B2 means that there are two different elements in a nonmetal bonded environment and both have two atoms. There are a total of three different types of this structure, depending on the distribution of identical elements, for a total of 108 possible structures. ABC2 represents a non-metallic environment with three elements, one of which has two atoms, and a total of 756 possibilities including three different types. ABCD represents the coordination environment containing four different nonmetals, with a total of 756 possible structures containing six different types. To sum up, there are 1701 possible environmental structures, which are listed in Table S1.

To accelerate the discovery process, we adopted a six-step screening strategy to obtain high-performance catalysts for CO_2RR based on stable configurations, as illustrated in Fig. 1b. Firstly, as CO was the key intermediate for various electrocatalytic products during CO_2RR, SACs with E_{ads}(CO) ranging from −0.3 eV to 0.3 eV were chosen to promote the formation of highly attractive multi-electron reduction chemicals. To promote CO_2 activation as well as subsequent electrocatalytic processes, we also looked for catalysts with negative CO_2 adsorption energies. Besides, we selected catalysts with $U_L(H_2)$ lower than −0.1 V to suppress the competing hydrogen evolution reactions (HER). Following that, to facilitate the desorption process of the generated products on the catalyst, we chose catalysts with product adsorption energies on the catalyst higher than −0.1 eV. After that, we revealed the mechanisms of products generation over different SACs and catalysts with high product selectivity were selected by choosing U_L(products) higher than $U_L(H_2)$. Finally, AIMD simulations at 300 K were performed to determine the kinetic stabilities of the selected SACs. Given that C–C coupling is a non-electroreduction process, the energy barrier of C–C coupling with a threshold of 0.75 eV was adopted to estimate if C_2 chemicals can be produced [43,44], which means the energy barrier of C–C coupling less than 0.75 eV will favour the production of C_2 chemicals. Through the above screening process, we will obtain high-performance catalysts for CO_2RR with high activity and selectivity.

3. Results

3.1. Establishment of stable SACs

The objective of this section is to screen stable SACs through sequentially designed environmental, central and axial ambient based on the Cu-N4 configuration.

At first, we designed the environmental NM based on Cu as the central atom and the possible 1701 structures are listed in Table S1. The calculated E_f and $E_{b\text{-}c}$ are shown in Table S2. Finally, we obtained 27 stable configurations as summarised in Table S3. Based on the above results, we changed their central M for a total of 675 possible structures (including Cu atom) and calculated their E_f and $E_{b\text{-}c}$ values. The 675 configurations and calculation results are presented in Fig. S4. After screening, 218 stable combinations were found as listed in Table S5. After that, we added 9 possible axial non-metallic atoms to the above structures thus a total of 1962 possible structures and evaluated their E_f and $E_{b\text{-}c}$ performance. The specific information is presented in Table S6. Finally, we screened 964 configurations with both negative E_f and $E_{b\text{-}c}$ values for further investigation, as shown in Table S7.

3.2. Identification of SACs with high activity for CO_2 reduction

Based on the above selection process, 964 novel SACs with high stability are found after considering 4311 possible configurations. In this part, we would further screen outstanding SACs with high activity for CO_2 reduction through E_{ads}(CO), $E_{ads}(CO_2)$, $U_L(H_2)$ and E_{ads}(products) values.

The adsorption energy of CO, E_{ads}(CO), is a crucial indicator for the screening of SACs as CO is an important intermediate for the production of C_1 and C_2 compounds (such as CH_3OH, CH_4, C_2H_6O, C_2H_4 and C_2H_6) during CO_2RR [45–47]. Generally speaking, CO is more likely to desorb from the catalyst and generate CO as the end product with weak CO adsorption on SACs. Strong CO adsorption will prevent further protonation processes producing high CO_2 reduction chemicals. Based on earlier research, the absorption energy of CO on Cu-N4 site is 0.3 eV [12]. That is a relatively weak E_{ads}(CO) and increasing CO adsorption on the SAC will favour the generation of valuable deep reduction products. According to earlier research, the adsorption of CO is recommended not to be lower than −0.3 eV to ensure the smoothness of the subsequent protonation process [18]. The calculated E_{ads}(CO) values of 964 stable configurations are listed in Table S8. Additionally, as illustrated in Table S9, a total of 244 SACs are discovered with E_{ads}(CO) ranging from −0.3 eV to 0.3 eV.

Furthermore, the adsorption and activation of CO_2 on catalysts is a challenge during CO_2RR because linear CO_2 molecules are stable and chemically inert, with low electron affinity and a wide energy gap [48,49]. To facilitate this process, catalysts with negative $E_{ads}(CO_2)$ are screened in [5]. The calculation results of CO_2 adsorption energy are presented in Table S10. Subsequently, 77 SACs with negative $E_{ads}(CO_2)$ values are found as summarized in Table S11.

Besides, HER is the primary side reaction during CO_2RR, which could reduce the efficiency of CO_2 reduction. We calculated the limiting potential of H_2 formation for the 77 selected catalysts, as shown in Table S12. We chose $U_L(H_2)$ values less than −0.1 V for the initial inhibition of HER and 67 potential catalysts were obtained and listed in Table S13.

Finally, the desorption of products from SACs to release active sites is an important indicator of catalytic performance. Too low values of E_{ads}(products) could prevent the detachment of generated products, so we chose catalysts with E_{ads}(products) greater than −0.1 eV to promote the quick release of products from the catalyst [18]. During CO_2RR, the main C_1 compounds in the CO_2 electroreduction process are HCOOH, CH_3OH, and CH_4. And for the key C_2 products, there are C_2H_4, C_2H_6, and C_2H_6O. According to the possible mechanisms for main chemicals during CO_2RR in our earlier work, the adsorption energies of HCOOH, CH_3OH, $H_2O\&CH_4$, C_2H_4, C_2H_6, and C_2H_6O are the indicators to estimate the desorption capacities of HCOOH, CH_3OH, CH_4, C_2H_4, C_2H_6, and C_2H_6O, respectively [12]. Since CO* is an important intermediate for products during CO_2RR except for HCOOH and the generation pathway is simple via $CO_2 \rightarrow CO_2^* \rightarrow COOH^* \rightarrow CO^*$, to accelerate the screening process, we further selected catalysts with U_L(CO) higher than $U_L(H_2)$ to ensure high selectivity for CO* generation during CO_2RR [50,51]. The U_L(CO) and $U_L(H_2)$ values of 67 SACs are shown in Table S14. And 14 SACs with U_L(CO) higher than $U_L(H_2)$ are discovered (Table S15). Table S16 presents adsorption energies of main products and SACs with E_{ads}(products) greater than −0.1 eV, which are found and summarised in Table S17.

3.3. Identification of SACs with high selectivity for CO_2 reduction

Following the screening process above, 47 SACs are discovered from 964 stable configurations that could benefit the formation of HCOOH, CH_4, C_2H_6 and C_2H_6O. The objective of this section is to reveal the underlying mechanisms during CO_2RR and obtain U_L(products) values. Fig. S2 depicts the reasonable reaction channels for target products generation, referring to previous research [12,52–54]. It should be emphasised that we only considered the potential routes for C_2H_6 and C_2H_6O formation for C_2 chemicals because no catalysts favourable for C_2H_4 were found in the screened 47 SACs. The most likely reaction route

is selected from the reaction network with the greatest U_L values. To guarantee the products selectivity during CO_2RR, SACs with $U_L(H_2)$ lower than U_L(products) are selected for further study, which can effectively inhibit the competitive response HER. Through calculations, we selected ten SACs that would benefit the generation of HCOOH, CH_4, C_2H_6 or C_2H_6O. Table S18 presents the detailed parameters for the

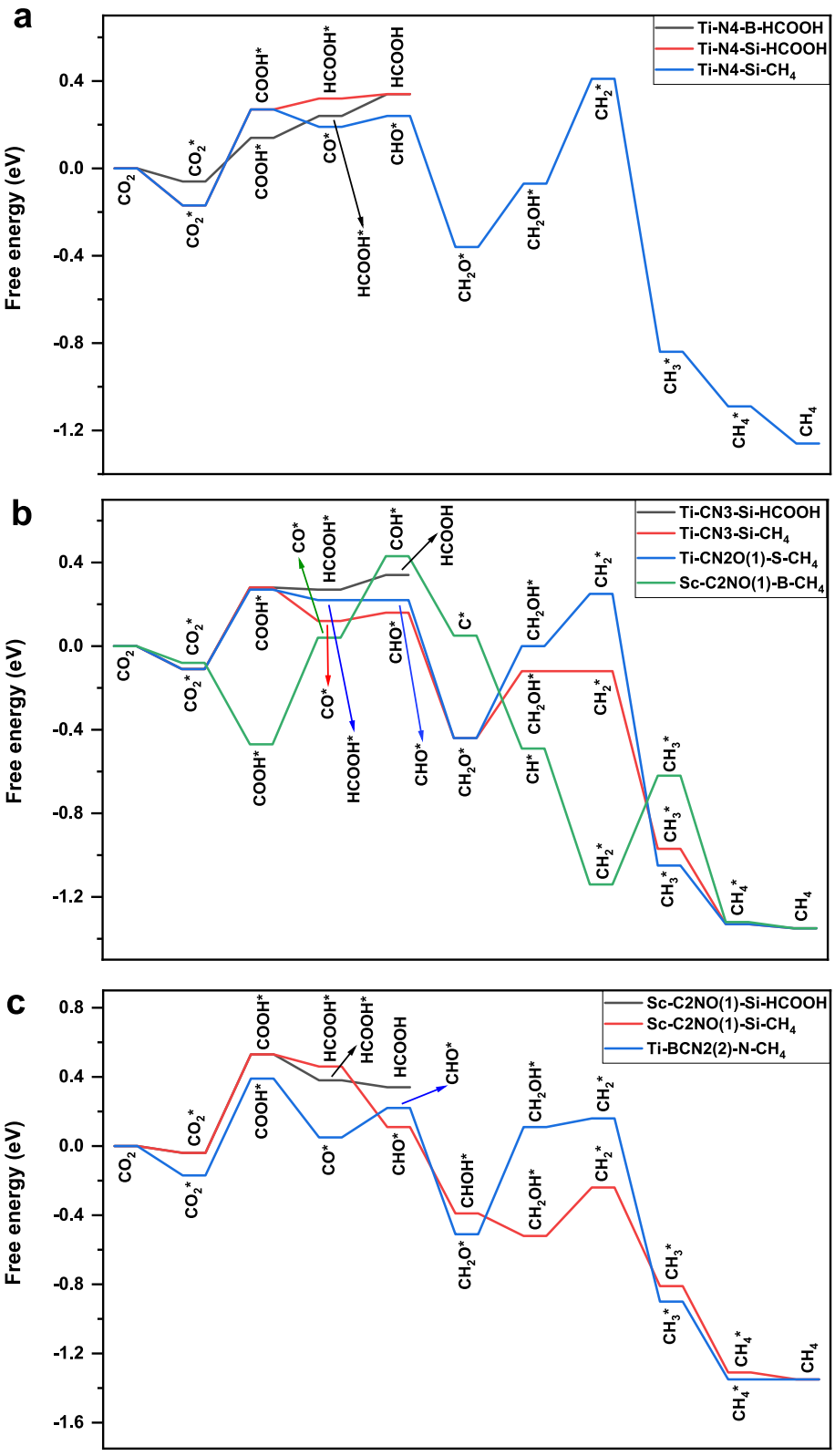

Fig. 2. Most favourable reaction pathways during CO_2 electroreduction to C_1 products at 0 applied voltage. (a) Ti-N4-B for HCOOH, Ti-N4-Si for HCOOH and Ti-N4-Si for CH_4; (b) Ti-CN3-Si for HCOOH, Ti-CN3-Si for CH_4, Ti-CN2O(1)-S for CH_4 and Sc-C2NO(1)-B for CH_4; (c) Sc-C2NO(1)-Si for HCOOH, Sc-C2NO(1)-Si for CH_4 and Ti-BCN2(2)-N for CH_4; (d) Sc-CN2O(3)-Si for HCOOH, Sc-CN2O(3)-Si for CH_4, Ru-C2NO(3)-C for CH_4 and Ti-BONC-C for CH_4 (symbol * means adsorbed state of intermediates).

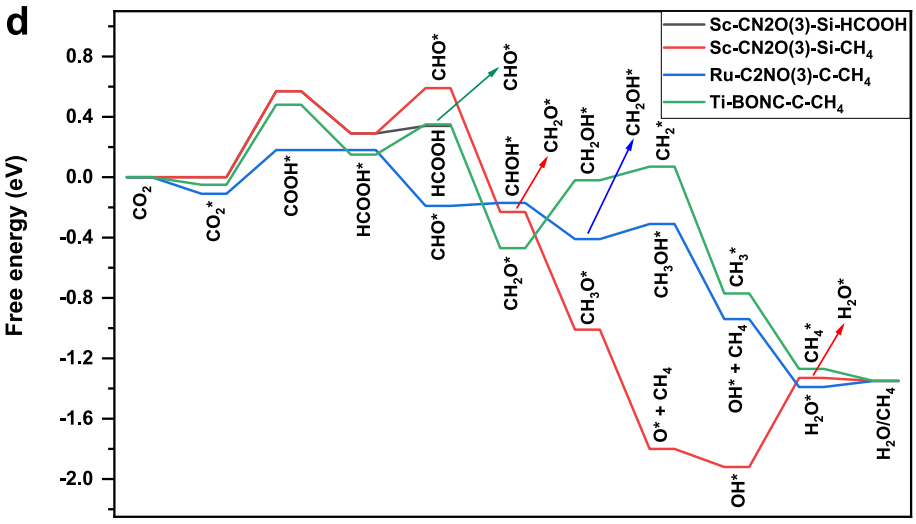

Fig. 2. (*continued*).

screening procedure.

3.3.1. CO_2RR mechanisms to C_1 chemicals

Fig. 2 illustrates the most favourable reaction routes during CO_2RR for HCOOH and CH_4. There are five SACs (Ti-N4-B, Ti-N4-Si, Ti-CN3-Si, Sc-C2NO(1)-Si and Sc-CN2O(3)-Si) benefit HCOOH formation with the common channel $CO_2 \rightarrow CO_2^* \rightarrow COOH^* \rightarrow HCOOH^* \rightarrow HCOOH$, the same limiting step of $CO_2^* \rightarrow COOH^*$ and limiting potentials of −0.2 V, −0.44 V, −0.39 V, −0.57 V and −0.57 V, respectively. Besides, a total of nine SACs are favourable for CH_4 generation, however, their formation mechanisms during CO_2RR change significantly on different SACs. The channel of CH_4 generation on Ti-N4-Si, Ti-CN3-S and Ti-BCN2(2)-N is $CO_2 \rightarrow CO_2^* \rightarrow COOH^* \rightarrow CO^* \rightarrow CHO^* \rightarrow CH_2O^* \rightarrow CH_2OH^* \rightarrow CH_2^* \rightarrow CH_3^* \rightarrow CH_4^* \rightarrow CH_4$. The limiting steps of Ti-N4-Si, Ti-CN3-S and Ti-BCN2(2)-N are $CH_2OH^* \rightarrow CH_2^*$, $CO_2^* \rightarrow COOH^*$ and $CO_2^* \rightarrow COOH^*$ with U_L of −0.48 V, −0.39 V and −0.56 V, respectively. The pathway $CO_2 \rightarrow CO_2^* \rightarrow COOH^* \rightarrow HCOOH^* \rightarrow CHO^* \rightarrow CH_2O^* \rightarrow CH_2OH^* \rightarrow CH_2^* \rightarrow CH_3^* \rightarrow CH_4^* \rightarrow CH_4$ is the common route for CH_4 generation on Ti-CN2O(1)-S and Ti-BONC-C with the limiting step is $CH_2O^* \rightarrow CH_2OH^*$($U_L = -0.44$ V) and $CO_2^* \rightarrow COOH^*$($U_L = -0.53$ V), respectively. $CO_2 \rightarrow CO_2^* \rightarrow COOH^* \rightarrow CO^* \rightarrow COH^* \rightarrow C^* \rightarrow CH^* \rightarrow CH_2^* \rightarrow CH_3^* \rightarrow CH_4^* \rightarrow CH_4$ is the channel generating CH_4 during CO_2RR on Sc-C2NO(1)-B with limiting step of $CH_2^* \rightarrow CH_3^*$ and U_L of −0.52 V. The routes for CH_4 formation on Sc-C2NO(1)-Si, Sc-CN2O(3)-Si and Ru-C2NO(3)-C are $CO_2 \rightarrow CO_2^* \rightarrow COOH^* \rightarrow HCOOH^* \rightarrow CHO^* \rightarrow CHOH^* \rightarrow CH^* \rightarrow CH_2^* \rightarrow CH_3^* \rightarrow CH_4^* \rightarrow CH_4$, $CO_2 \rightarrow CO_2^* \rightarrow COOH^* \rightarrow HCOOH^* \rightarrow CHO^* \rightarrow CH_2O^* \rightarrow CH_3O^* \rightarrow O^* \rightarrow OH^* \rightarrow H_2O^* \rightarrow H_2O$ and $CO_2 \rightarrow CO_2^* \rightarrow COOH^* \rightarrow HCOOH^* \rightarrow CHO^* \rightarrow CH_2O^* \rightarrow CH_2OH^* \rightarrow CH_3OH^* \rightarrow OH^* \rightarrow H_2O^* \rightarrow H_2O$, respectively. $CO_2^* \rightarrow COOH^*$ is the common limiting step for Sc-C2NO(1)-Si and Sc-CN2O(3)-Si with U_L of −0.57 V and −0.29 V, respectively. The limiting step and limiting potential for Sc-CN2O(3)-Si are $OH^* \rightarrow H_2O^*$ and −0.59 V, respectively. The relevant free energies of elementary reactions are listed in Table S19.

3.3.2. CO_2RR mechanisms to C_2 chemicals

After screening, we found a total of seven catalysts (Ti-N4-Si, Ti-CN2O(1)-S, Sc-C2NO(1)-B, Sc-C2NO(1)-Si, Ti-BCN2(2)-N, Sc-CN2O(3)-Si and Ti-BNOC-C) that can promote the production of C_2 products under the condition U_L(products) higher than $U_L(H_2)$. However, C–C coupling is a non-electrochemical process and the energy barrier (G_b) determines whether the C–C bond can be generated at room temperature with a threshold of 0.75 eV [43,55]. Based on previous studies [31,56], CO*–CO*, CO*–CHO* and CO*–COH* are the three routes during CO_2RR. Among them, CO*–COH* is not considered for Ti-N4-Si, Ti-CN2O(1)-S, Sc-C2NO(1)-Si, Ti-BCN2(2)-N, Sc-CN2O(3)-Si and Ti-BNOC-C as the formation of COH* by CO* → COH* is difficult with free energy changes of 1.71 eV, 1.82 eV, 1.28 eV, 1.71 eV, 2.38 eV and 1.47 eV, respectively. CO*–CO* coupling is not realistic for Ti-BNOC-C as the free energy change from 2CO* to CO-CO* is 1.45 eV, which is significantly higher than 0.75 eV. As observed in Fig. 3, the C–C bond generation on Ti-N4-Si, Ti-CN2O(1)-S and Sc-CN2O(3)-Si is inhibited by high energy barriers during the C–C coupling process. CO*–CHO* is the most favourable coupling pathway for Sc-C2NO(1)-Si, Ti-BCN2(2)-N and Ti-BNOC-C with G_b of 0.11 eV, 0.62 eV and 0.26 eV, respectively. The most favourable C–C coupling channel for Sc-C2NO(1)-B is CO*–COH* with G_b of 0.16 eV.

As shown in Fig. 4, the reaction channels for CH_3CH_2OH generation on Sc-C2NO(1)-B and Sc-C2NO(1)-Si are $CO_2 \rightarrow CO_2^* \rightarrow COOH^* \rightarrow CO^* \rightarrow COH^* \rightarrow CO\text{-}COH^* \rightarrow C\text{-}CO^* \rightarrow C\text{-}CHO^* \rightarrow CH\text{-}CHO^* \rightarrow CH\text{-}CHOH^* \rightarrow CH_2\text{-}CHOH^* \rightarrow CH_2\text{-}CH_2OH^* \rightarrow CH_3\text{-}CH_2OH^* \rightarrow CH_3\text{-}CH_2OH$ and $CO_2 \rightarrow CO_2^* \rightarrow COOH^* \rightarrow CO^* \rightarrow CHO^* \rightarrow CO\text{-}CHO^* \rightarrow CHO\text{-}COH^* \rightarrow$

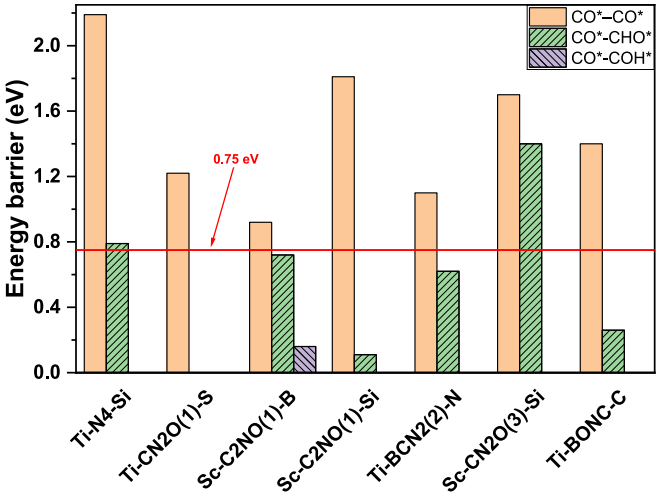

Fig. 3. Energy barriers of C–C coupling process on Ti-N4-Si, Ti-CN2O(1)-S, Sc-C2NO(1)-B, Sc-C2NO(1)-Si, Ti-BCN2(2)-N, Sc-CN2O(3)-Si and Ti-BNOC-C.

CHOH-COH*→ CH-COH* → CH_2-COH* → CH_2-CHOH* → CH_2-CH_2OH* → CH_3-CH_2OH* → CH_3-CH_2OH, respectively. CO_2 → CO_2* → COOH* → CO* → CHO* → CO-CHO* → CHO-COH* → C-CHO*→ CH-CHO* → CH-CHOH* → CH_2-CHOH* → CH_2-CH_2OH* → CH_3-CH_2OH* → CH_3-CH_2OH is the common pathway for Ti-BCN2(2)-N and Ti-BONC-C during CO_2RR for CH_3-CH_2OH formation. COOH* → CO* is the limiting step for the above four SACs with U_L of −0.51 V (Sc-C2NO(1)-B), −0.57 V (Sc-C2NO (1)-Si), −0.56 V (Ti-BCN2(2)-N) and −0.53 V (Ti-BONC-C). The relevant free energies of elementary reactions for CH_3CH_2OH formation are listed in Table S20.

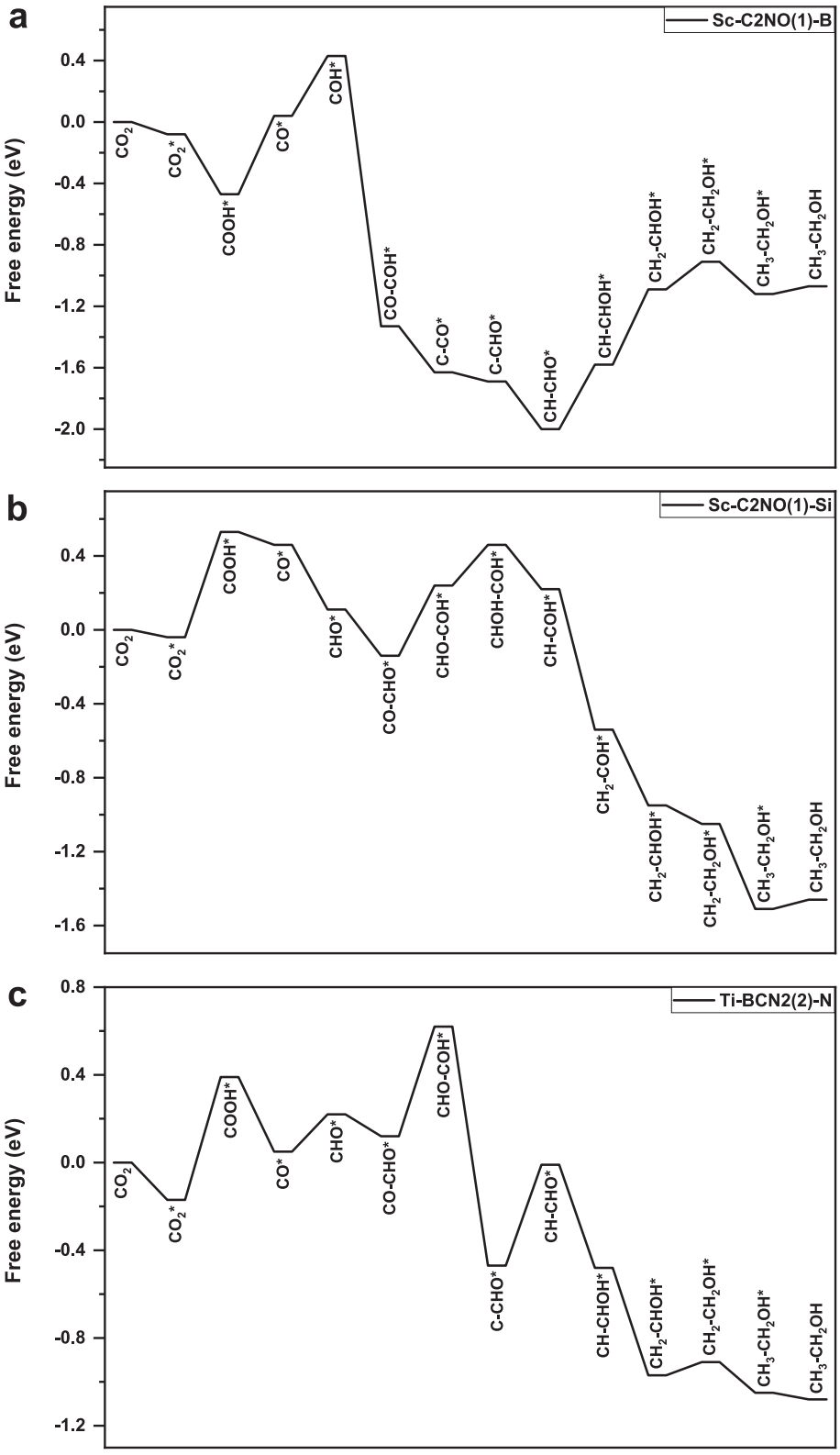

Fig. 4. Most favourable reaction pathways during CO_2 electroreduction to CH_3CH_2OH products at 0 applied voltage. (a) Sc-C2NO(1)-B, (b) Sc-C2NO(1)-Si, (c) Ti-BCN2(2)-N and (d) Ti-BONC-C (symbol * means adsorbed state of intermediates).

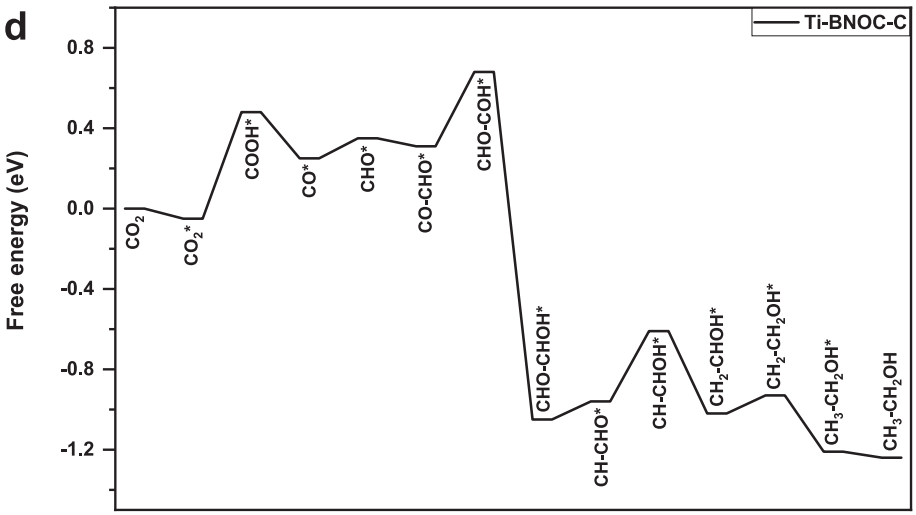

Fig. 4. (*continued*).

3.4. Kinetic stability analysis and summary of developed SACs

A series of 10 ps AIMD simulations at 300 K with a timestep of 0.5 fs are carried out for the discovered SACs to estimate their kinetic stabilities. Fig. S3 illustrates the initial and final configurations during the AIMD simulations. Although the above SACs undergo some alterations after the simulations, there are still strong interactions between the environmental NM, central M and axial NM and no obvious structural deformations have been observed. Therefore, these ten potential SACs have high kinetic stabilities.

As shown in Table 1, the screened catalysts exhibit a significant enhancement in C_2H_6O selectivity compared to previously reported SACs. This improvement is attributed to their higher $U_L(C_2H_6O)$ relative to $U_L(H_2)$. During CO_2RR, the external applied voltages required for the formation of HCOOH, CH_4, and C_2H_6O are reduced by 45 % (Ti-N_4-B), 71 % (Ru-C_2NO(3)-C), and 48 % (Sc-C_2NO(1)-B), respectively, compared to the best-performing catalysts reported in the literature (Cu-N_4 and Os-N_4-O). From the perspective of limiting potential, Ti-N4-Si is more favourable to HCOOH generation due to the higher U_L value than that of CH_4. Similarly, C_2H_6O is more easily to produce on Sc-C2NO(1)-B than CH_4 due to its higher limiting potential value.

3.5. Electronic analysis

On the basis of the above conclusions, the CO_2RR behaviours of SACs can be efficiently improved through changing environmental NM, central M and axial NM. Compared with Cu-N4 site, the novel designed catalysts significantly promote CO_2 adsorption and decrease the required external applied voltage for products generation. During CO_2RR, CO_2 protonation is usually the limiting step for most SACs. CO_2 protonation prefers the CO* → OCHO* route for Cu-N4 [12], however, CO* → COOH* is the favourable pathway for the discovered catalysts. To explain the above phenomenon in depth, Ti-N4-B is selected with the highest U_L among the found SACs for electronic analysis through charge density difference (CDD) and partial density of states (PDOS) and Crystal orbital Hamilton population (COHP) analysis.

Fig. 5 shows charge density difference of adsorbed CO_2, COOH and OCHO on Cu-N4 and Ti-N4-B, respectively. The position numbers and Bader chargers of relevant atoms are shown in Fig. S4 and Table S21, respectively. Overall, electrons transfer from Cu-N4 catalyst to adsorbate with 0.02 electrons to CO_2 (Cu–N), 1.04 electrons to COOH (Cu-C) and 0.91 electrons to OCHO (Cu-O1), respectively. However, for Ti-N4-B site, CO_2, COOH and OCHO transfer 0.82, 0.51 and 1.58 charges to the substrate through bonds Ti–O1&TiC, Ti–O1&Ti–C and Ti–O2, respectively. It is obvious that the number of charge transfers during CO_2 adsorption on Ti-N4-B was significantly higher than that on Cu-N4, implying that the adsorption of Ti-N4-B for CO_2 is stronger. Thus, the adsorption of CO_2 on Ti-N4-B (−0.06 eV) is lower than Cu–N (0.32 eV). For the CO_2 protonation process, OCHO transfers more electrons to the substrate during adsorption onto Ti-N4-B than COOH, resulting in a lower adsorption energy for OCHO (−2.76 eV) than COOH (0.2 eV). However, the adsorption of COOH and OCHO on Cu-N4 showed an opposite pattern, with more charge transfer during adsorption and higher adsorption energy for COOH (1.07 eV) compared to OCHO (0.44

Table 1
Summary of U_L of the key products during the CO_2RR on Cu-N4 [12], Ni-N4 [14], Fe-N4 [14], Co-N4 [14], Ni-N3B [16], Mn-N4-C [20], Cr-N4-C [20], Os-N4-O [20], Ru-N4-O [20], Rh-N4-O [20], Ti-N4-B, Ti-N4-Si, Ti-CN3-Si, Ti-CN2O(1)-S, Sc-C2NO(1)-B, Sc-C2NO(1)-Si, Ti-BCN2(2)-N, Sc-CN2O(3)-Si, Ru-C2NO(3)-C and Ti-BONC-C.

Name	H_2	HCOOH	CH_4	C_2H_6O	Name	H_2	HCOOH	CH_4	C_2H_6O
Cu-N4	−0.8	−0.44	−0.68	−1.07	Ti-N4-B	−0.42	−0.2	–	–
Ni-N4	–	−1.511	–	–	Ti-N4-Si	−0.52	−0.44	−0.48	–
Fe-N4	–	–	−0.877	–	Ti-CN3-Si	−0.46	−0.39	−0.39	–
Co-N4	–	–	−0.687	–	Ti-CN2O(1)-S	−0.52	–	−0.38	–
Ni-N3B	–	–	−0.42	–	Sc-C2NO(1)-B	−0.77	–	−0.52	−0.51
Mn-N4-C	–	–	−0.49	–	Sc-C2NO(1)-Si	−0.6	−0.57	−0.57	−0.57
Cr-N4-C	–	–	−0.54	–	Ti-BCN2(2)-N	−0.66	–	−0.56	−0.56
Os-N4-O	–	–	−0.41	–	Sc-CN2O(3)-Si	−0.63	−0.57	−0.57	–
Ru-N4-O	–	–	−0.58	–	Ru-C2NO(3)-C	−0.68	–	−0.29	–
Rh-N4-O	–	–	−0.68	–	Ti-BONC-C	−0.66	–	−0.53	−0.53

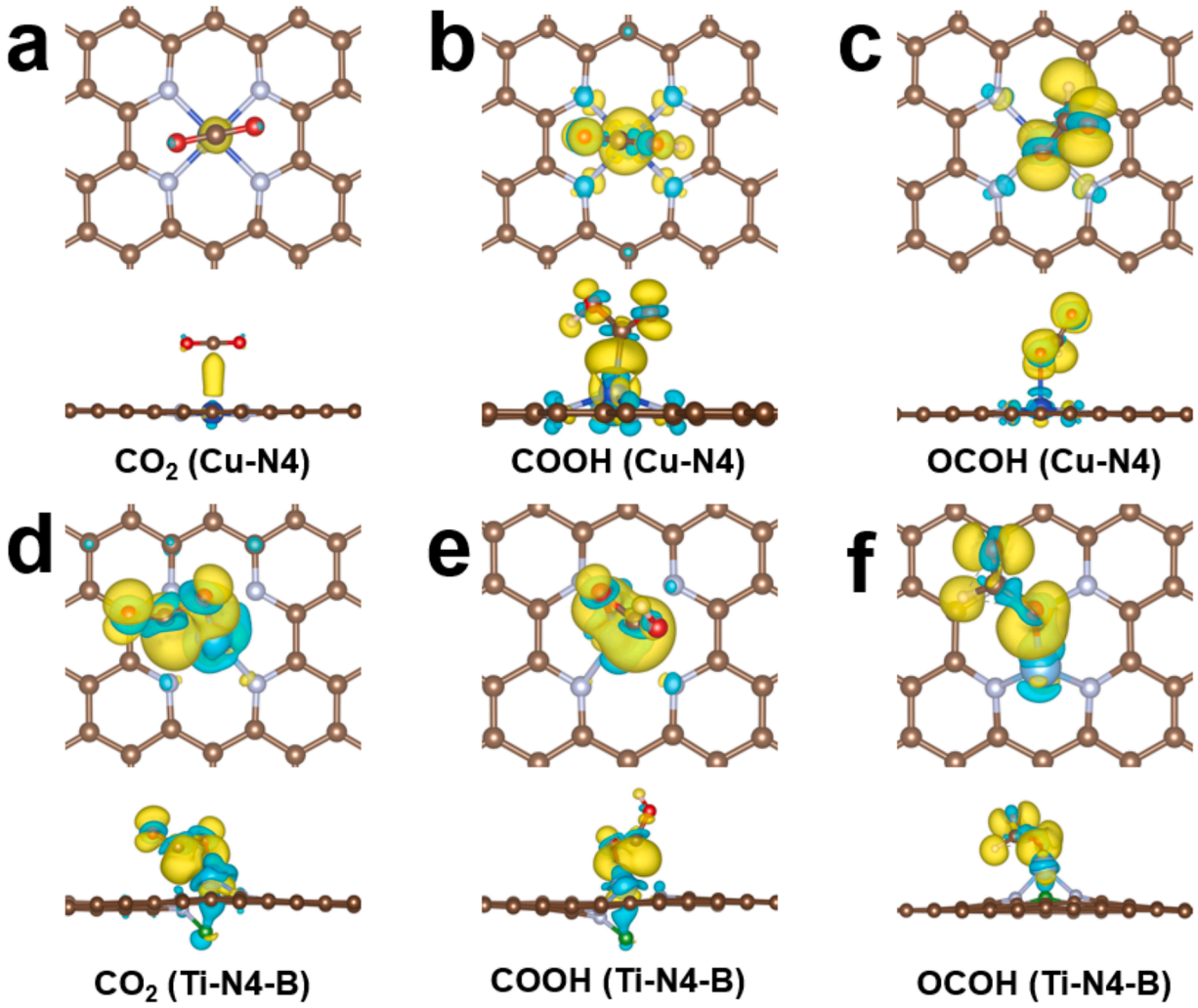

Fig. 5. Charge density difference of adsorbed intermediates on catalysts. (a) CO_2 on Cu-N4, (b) COOH on Cu-N4 [12], (c) OCOH on Cu-N4, (d) CO_2 on Ti-N4-B, (e) COOH on Ti-N4-B and (f) OCOH on Ti-N4-B. The isosurface value is 0.001 e $bohr^{-3}$ on Fig. 6a. The isosurface values are 0.004 e $bohr^{-3}$ on Fig. 6b–f. Yellow and blue regions mean increasing and decreasing electron densities, respectively. (For interpretation of the references to colour in this figure legend, the reader is referred to the web version of this article.)

eV). This may be due to the different types of bonds in the adsorption process between COOH (Cu–C bond) and OCHO (Cu–O bond). And PDOS and COHP analyses are carried out to further explain the changes in adsorption energy of different intermediates on catalysts.

As observed in Fig. 5, the active sites of the adsorbed intermediates on both Cu-N4 and Ti-N4-B catalysts are the central atoms. Fig. 6a illustrates the PDOS results of Cu and Ti atoms to estimate the adsorption energy of adsorbates on catalysts. Ti has significantly higher d-band centre than Cu atom, which is 0.4 eV and −3.1 eV, respectively. Thus, Ti atom has higher activity than Cu atom and adsorbs more strongly to intermediates, which is consistent with the phenomenon that the adsorption energy of adsorbates on Ti-N4-B is lower than that of Cu–N4. According to Fig. 6b and c, the interaction between the p-orbital of O atom and the d-orbital of Cu atom is stronger than the p-orbital of C atom. Thus, the Cu–O bond is more stable than the Cu–C bond and the adsorption energy of OCHO is lower than that of COOH. Similarly, the orbital bonding of O-p with Ti-d is stronger than that of C-p during COOH adsorption on Ti-N4-B (Fig. 6d), indicating that the Ti–O bond contributes more to the adsorption energy during COOH adsorption. During OCHO adsorption, only Ti–O bonds are generated, and the interactions between O-p and Ti-d orbitals are stronger than during COOH adsorption, as illustrated in Fig. 6e. Compared to the O–P orbital in Fig. 6d, the O–P orbital in Fig. 6e has a higher peak value and is closer to the Fermi energy level. Thus, the Ti–O bond during OCHO adsorption is stronger than that during COOH adsorption. Considering the lower adsorption energy of OCHO, the contribution of Ti–O bond during OCHO adsorption is higher than the contribution of Ti–C and Ti–O bonds to the adsorption energy during COOH adsorption.

COHP calculations are performed during CO_2, COOH and OCHO adsorption on Cu-N4 and Ti-N4-B catalysts to quantitatively assess the strength of various chemical bonds. The -integrated-COHP(−ICOHP) values are listed in Fig. 6f. In general, the larger the value of -ICOHP, the stronger the bonding between the two atoms. During CO_2 and COOH adsorption, one more bond will be generated on Ti-N4-B (Ti–O) than on Cu-N4, and the –ICOHP values of Ti–C are all higher than those of Cu–C. Also, the –ICOHP values of Ti–O are all higher than those of Cu–O during OCHO adsorption. Those results imply that, compared to Cu-N4, CO_2, COOH and OCHO are more strongly adsorbed on Ti-N4-B with lower adsorption energies, consistent with the above findings.

To sum up, it can be concluded that OCHO has a lower adsorption energy on catalysts than COOH because of the generation of the strong metal-O bond. Therefore, CO_2 protonation prefers the CO* → OCHO* route for Cu-N4. However, for Ti-N4-B, the too strong OCHO adsorption inhibits the subsequent protonation process, so that the CO* → COOH* pathway is more likely to occur on Ti-N4-B.

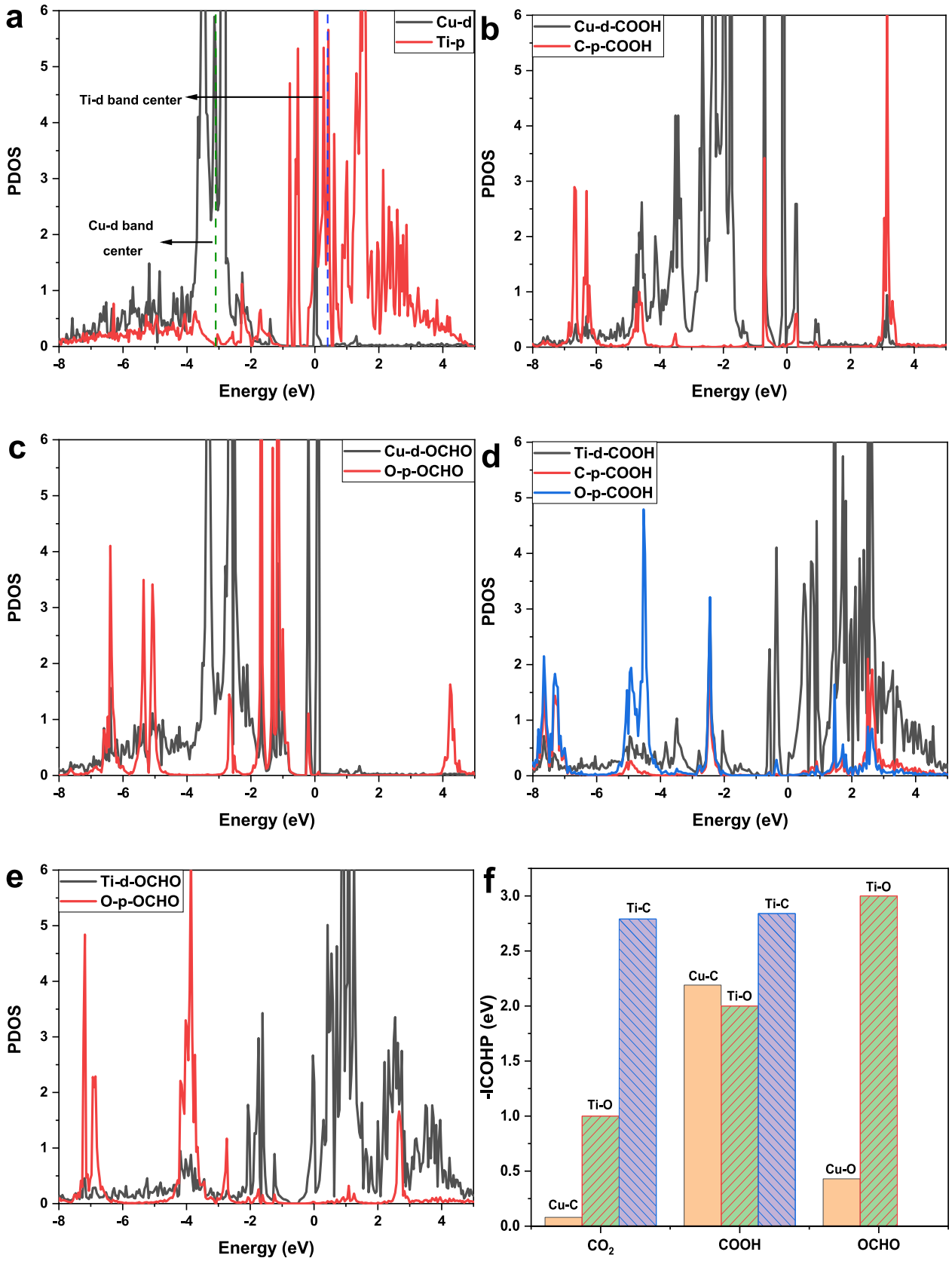

Fig. 6. Partial density of states (PDOS) of (a) Cu and Ti on Cu-N4 and Ti-N4-B, (b) Cu and C on Cu-N4-COOH, (c) Cu and O on Cu-N4-OCOH, (d) Ti, C and O on Ti-N4-B-COOH, (e) Ti and O on Ti-N4-B-OCOH. (f) –ICOHP values of relevant bonds during the adsorption of CO_2, COOH and OCHO on Cu-N4 and Ti-N4-B.

4. Conclusions

In summary, we designed novel single-atom catalysts (SACs) by modifying environmental nonmetals, central atoms, and axial nonmetals through DFT calculations. After screening 4311 configurations, we identified 10 optimal SACs that demonstrate high activity and selectivity for HCOOH, CH_4, and C_2H_6O production. Specifically, the externally applied voltages required for the formation of HCOOH, CH_4, and C_2H_6O were reduced by 45 % (Ti-N_4-B), 71 % (Ru-C_2NO(3)-C), and 48 % (Sc-C_2NO(1)-B), respectively, compared to the best-performing catalysts reported in the literature (Cu-N_4 [12] and Os-N_4-O [20]). The improved performance is attributed to the rational design of environmental nonmetals, central atoms, and axial nonmetals, which is further supported by electronic analysis. Our work provides a new design principle for efficiently screening SACs with high activity and selectivity for CO_2RR, offering valuable insights into reaction mechanisms. Future efforts will focus on experimental validation and potential industrial application of discovered promising catalysts. Moreover, combining DFT with machine learning (ML) will help further improve computational efficiency, accelerate the discovery of catalysts and uncover hidden patterns behind the performance of high-efficiency catalysts for CO_2RR.

CRediT authorship contribution statement

Zhongze Bai: Writing – original draft, Visualization, Validation, Software, Methodology, Investigation, Formal analysis, Data curation, Conceptualization. **Xi Zhuo Jiang:** Writing – review & editing, Supervision. **Kai H. Luo:** Writing – review & editing, Supervision, Resources, Project administration, Funding acquisition.

Declaration of competing interest

The authors declare that they have no known competing financial interests or personal relationships that could have appeared to influence the work reported in this paper.

Acknowledgements

Support from the UK Engineering and Physical Sciences Research Council under Grant Nos. EP/T015233/1 and EP/X035875/1 is gratefully acknowledged. This work made use of computational support by CoSeC, the Computational Science Centre for Research Communities, through UKCOMES.

Appendix A. Supplementary data

Supplementary data to this article can be found online at https://doi.org/10.1016/j.jcis.2025.02.015.

Data availability

Data will be made available on request.

References

[1] S.N. Talapaneni, G. Singh, I.Y. Kim, K. AlBahily, A.-M. AaH, A.S. Karakoti, et al., Nanostructured carbon nitrides for CO2 capture and conversion, Adv. Mater. 32 (18) (2020) 1904635.
[2] Z. Feng, G. Su, H. Ding, Y. Ma, Y. Li, Y. Tang, et al., Atomic alkali metal anchoring on graphdiyne as single-atom catalysts for capture and conversion of CO2 to HCOOH, Mol. Catal. 494 (2020) 111142.
[3] X. Bai, Q. Li, L. Shi, X. Niu, C. Ling, J. Wang, Hybrid Cu0 and Cux+ as atomic interfaces promote high-selectivity conversion of CO2 to C2H5OH at low potential, Small 16 (12) (2020) 1901981.
[4] M. Umer, S. Umer, R. Anand, J. Mun, M. Zafari, G. Lee, et al., Transition metal single atom embedded GaN monolayer surface for efficient and selective CO 2 electroreduction, J. Mater. Chem. A 10 (45) (2022) 24280–24289.
[5] X. Wei, S. Wei, S. Cao, Y. Hu, S. Zhou, S. Liu, et al., Cu acting as Fe activity promoter in dual-atom Cu/Fe-NC catalyst in CO2RR to C1 products, Appl. Surf. Sci. 564 (2021) 150423.
[6] X. Li, Z. Wang, J. Zhang, K. Dai, K. Fan, G. Dawson, Branch-like CdxZn1-xSe/Cu2O@ Cu step-scheme heterojunction for CO2 photoreduction, Mater. Today Phys. 26 (2022) 100729.
[7] M. Liu, M. Peng, B. Dong, Y. Teng, L. Feng, Q. Xu, Explicating the role of metal centers in porphyrin-based MOFs of PCN-222 (M) for electrochemical reduction of CO2, Chin. J. Struct. Chem. 41 (7) (2022) 2207046–2207052.
[8] C.-P. Wan, J.-D. Yi, R. Cao, Y.-B. Huang, Conductive Metal/Covalent Organic Frameworks for CO2 Electro-reduction, Chin. J. Struct. Chem. 41 (5) (2022) 2205001–2205014.
[9] W. Zou, R. Lu, X. Liu, G. Xiao, X. Liao, Z. Wang, et al., Theoretical insights into dual-atom catalysts for the oxygen reduction reaction: the crucial role of orbital polarization, J. Mater. Chem. A 10 (16) (2022) 9150–9160.
[10] H. Sun, Y. Li, L. Gao, M. Chang, X. Jin, B. Li, et al., High throughput screening of single atomic catalysts with optimized local structures for the electrochemical oxygen reduction by machine learning, J. Energy Chem. 81 (2023) 349–357.
[11] B. Zhang, B. Zhang, Y. Jiang, T. Ma, H. Pan, W. Sun, Single-atom electrocatalysts for multi-electron reduction of CO2, Small 17 (36) (2021) 2101443.
[12] Z. Bai, X.Z. Jiang, K.H. Luo, Theoretical exploration on the performance of single and dual-atom Cu catalysts on the CO 2 electroreduction process: a DFT study, PCCP 25 (35) (2023) 23717–23727.
[13] G. Qu, K. Wei, K. Pan, J. Qin, J. Lv, J. Li, et al., Emerging materials for electrochemical CO 2 reduction: progress and optimization strategies of carbon-based single-atom catalysts, Nanoscale 15 (8) (2023) 3666–3692.
[14] Y. Yang, J. Li, C. Zhang, Z. Yang, P. Sun, S. Liu, et al., Theoretical insights into nitrogen-doped graphene-supported Fe Co, and Ni as single-atom catalysts for CO2 reduction reaction, J. Phys. Chem. C 126 (9) (2022) 4338–4346.
[15] Z. Wang, C. Wang, Y. Hu, S. Yang, J. Yang, W. Chen, et al., Simultaneous diffusion of cation and anion to access N, S co-coordinated Bi-sites for enhanced CO 2 electroreduction, Nano Res. 1–7 (2021).
[16] Z. Fu, Q. Li, X. Bai, Y. Huang, L. Shi, J. Wang, Promoting the conversion of CO 2 to CH 4 via synergistic dual active sites, Nanoscale 13 (28) (2021) 12233–12241.
[17] K. Li, S. Zhang, X. Zhang, S. Liu, H. Jiang, T. Jiang, et al., Atomic tuning of single-atom Fe–N–C catalysts with phosphorus for robust electrochemical CO2 reduction, Nano Lett. 22 (4) (2022) 1557–1565.
[18] A. Chen, X. Zhang, L. Chen, S. Yao, Z. Zhou, A machine learning model on simple features for CO2 reduction electrocatalysts, J. Phys. Chem. C 124 (41) (2020) 22471–22478.
[19] M. Huang, B. Deng, X. Zhao, Z. Zhang, F. Li, K. Li, et al., Template-sacrificing synthesis of well-defined asymmetrically coordinated single-atom catalysts for highly efficient CO2 electrocatalytic reduction, ACS Nano 16 (2) (2022) 2110–2119.
[20] J. Wang, M. Zheng, X. Zhao, W. Fan, Structure-performance descriptors and the role of the axial oxygen atom on M–N4–C single-atom catalysts for electrochemical CO2 reduction, ACS Catal. 12 (9) (2022) 5441–5454.
[21] J.-X. Peng, W. Yang, Z. Jia, L. Jiao, H.-L. Jiang, Axial coordination regulation of MOF-based single-atom Ni catalysts by halogen atoms for enhanced CO2 electroreduction, Nano Res. 15 (12) (2022) 10063–10069.
[22] G. Kresse, J. Furthmüller, Efficiency of ab-initio total energy calculations for metals and semiconductors using a plane-wave basis set, Comput. Mater. Sci 6 (1) (1996) 15–50.
[23] G. Kresse, J. Hafner, Ab initio molecular dynamics for liquid metals, Phys. Rev. B 47 (1) (1993) 558.
[24] B. Hammer, L.B. Hansen, J.K. Nørskov, Improved adsorption energetics within density-functional theory using revised Perdew-Burke-Ernzerhof functionals, Phys. Rev. B 59 (11) (1999) 7413.
[25] P.E. Blöchl, Projector augmented-wave method, Phys. Rev. B 50 (24) (1994) 17953.
[26] S. Grimme, J. Antony, S. Ehrlich, H. Krieg, A consistent and accurate ab initio parametrization of density functional dispersion correction (DFT-D) for the 94 elements H-Pu, J. Chem. Phys. 132 (15) (2010) 154104.
[27] S. Grimme, S. Ehrlich, L. Goerigk, Effect of the damping function in dispersion corrected density functional theory, J. Comput. Chem. 32 (7) (2011) 1456–1465.
[28] K. Mathew, V.C. Kolluru, S. Mula, S.N. Steinmann, R.G. Hennig, Implicit self-consistent electrolyte model in plane-wave density-functional theory, J. Chem. Phys. 151 (23) (2019) 234101.
[29] K. Letchworth-Weaver, T. Arias, Joint density functional theory of the electrode-electrolyte interface: Application to fixed electrode potentials, interfacial capacitances, and potentials of zero charge, Phys. Rev. B 86 (7) (2012) 075140.
[30] K. Mathew, R. Sundararaman, K. Letchworth-Weaver, T. Arias, R.G. Hennig, Implicit solvation model for density-functional study of nanocrystal surfaces and reaction pathways, J. Chem. Phys. 140 (8) (2014) 084106.
[31] A.J. Garza, A.T. Bell, M. Head-Gordon, Mechanism of CO2 reduction at copper surfaces: pathways to C2 products, ACS Catal. 8 (2) (2018) 1490–1499.
[32] J.K. Nørskov, J. Rossmeisl, A. Logadottir, L. Lindqvist, J.R. Kitchin, T. Bligaard, et al., Origin of the overpotential for oxygen reduction at a fuel-cell cathode, J. Phys. Chem. B 108 (46) (2004) 17886–17892.
[33] A.A. Peterson, F. Abild-Pedersen, F. Studt, J. Rossmeisl, J.K. Nørskov, How copper catalyzes the electroreduction of carbon dioxide into hydrocarbon fuels, Energ. Environ. Sci. 3 (9) (2010) 1311–1315.
[34] G. Henkelman, B.P. Uberuaga, H. Jónsson, A climbing image nudged elastic band method for finding saddle points and minimum energy paths, J. Chem. Phys. 113 (22) (2000) 9901–9904.

[35] V. Wang, N. Xu, J.-C. Liu, G. Tang, W.-T. Geng, VASPKIT: A user-friendly interface facilitating high-throughput computing and analysis using VASP code, Comput. Phys. Commun. 267 (2021) 108033.
[36] W. Yi, G. Tang, X. Chen, B. Yang, X. Liu, qvasp: A flexible toolkit for VASP users in materials simulations, Comput. Phys. Commun. 257 (2020) 107535.
[37] S. Maintz, V.L. Deringer, A.L. Tchougréeff, R. Dronskowski, LOBSTER: A Tool to Extract Chemical Bonding from Plane-Wave Based DFT, Wiley Online Library, 2016.
[38] S. Zhu, K. Wan, H. Wang, L.-J. Guo, X. Shi, The role of supported dual-atom on graphitic carbon nitride for selective and efficient CO2 electrochemical reduction, Nanotechnology 32 (38) (2021) 385404.
[39] C. Guo, T. Zhang, X. Deng, X. Liang, W. Guo, X. Lu, et al., Electrochemical CO2 reduction to C1 products on single nickel/cobalt/iron-doped graphitic carbon nitride: a DFT study, ChemSusChem 12 (23) (2019) 5126–5132.
[40] S. Back, Y. Jung, TiC-and TiN-supported single-atom catalysts for dramatic improvements in CO2 electrochemical reduction to CH4, ACS Energy Lett. 2 (5) (2017) 969–975.
[41] J.H. Montoya, C. Tsai, A. Vojvodic, J.K. Nørskov, The challenge of electrochemical ammonia synthesis: a new perspective on the role of nitrogen scaling relations, ChemSusChem 8 (13) (2015) 2180–2186.
[42] R. Hu, Y. Li, Q. Zeng, J. Shang, Role of active sites in N-coordinated Fe-Co dual-metal doped graphene for oxygen reduction and evolution reactions: A theoretical insight, Appl. Surf. Sci. 525 (2020) 146588.
[43] D. Chen, Z. Chen, Z. Lu, J. Tang, X. Zhang, C.V. Singh, Computational screening of homo and hetero transition metal dimer catalysts for reduction of CO 2 to C 2 products with high activity and low limiting potential, J. Mater. Chem. A 8 (40) (2020) 21241–21254.
[44] J.H. Montoya, C. Shi, K. Chan, J.K. Nørskov, Theoretical insights into a CO dimerization mechanism in CO2 electroreduction, J. Phys. Chem. Lett. 6 (11) (2015) 2032–2037.
[45] M.G. Kibria, J.P. Edwards, C.M. Gabardo, C.T. Dinh, A. Seifitokaldani, D. Sinton, et al., Electrochemical CO2 reduction into chemical feedstocks: from mechanistic electrocatalysis models to system design, Adv. Mater. 31 (31) (2019) 1807166.
[46] A.A. Peterson, J.K. Nørskov, Activity descriptors for CO2 electroreduction to methane on transition-metal catalysts, J. Phys. Chem. Lett. 3 (2) (2012) 251–258.
[47] X. Liu, J. Xiao, H. Peng, X. Hong, K. Chan, J.K. Nørskov, Understanding trends in electrochemical carbon dioxide reduction rates, Nat. Commun. 8 (1) (2017) 15438.
[48] S. Xu, E.A. Carter, Theoretical insights into heterogeneous (photo) electrochemical CO2 reduction, Chem. Rev. 119 (11) (2018) 6631–6669.
[49] L. Fu, R. Wang, C. Zhao, J. Huo, C. He, K.-H. Kim, et al., Construction of Cr-embedded graphyne electrocatalyst for highly selective reduction of CO2 to CH4: A DFT study, Chem. Eng. J. 414 (2021) 128857.
[50] Y. Wang, R. Xie, N. Ci, Z. Zhu, C. Li, G. Chai, et al., Modified Cu active sites by alloying for efficient electrocatalytic reduction CO2 to CO, J. Energy Chem. 99 (2024) 450–457.
[51] Y. Luo, J. Yang, J. Qin, K. Miao, D. Xiang, A. Kuchkaev, et al., Cobalt phthalocyanine promoted copper catalysts toward enhanced electro reduction of CO2 to C2: Synergistic catalysis or tandem catalysis? J. Energy Chem. 92 (2024) 499–507.
[52] J.H. Liu, L.M. Yang, E. Ganz, Two-dimensional organometallic TM3–C12S12 monolayers for electrocatalytic reduction of CO2, Energy Environ. Mater. 2 (3) (2019) 193–200.
[53] S. Wang, W. Ma, Z. Sang, F. Hou, W. Si, J. Guo, et al., Dual-modification of manganese oxide by heterostructure and cation pre-intercalation for high-rate and stable zinc-ion storage, J. Energy Chem. 67 (2022) 82–91.
[54] S. Liu, B. Zhang, L. Zhang, J. Sun, Rational design strategies of Cu-based electrocatalysts for CO2 electroreduction to C2 products, J. Energy Chem. (2022).
[55] H. Li, D. Wu, J. Wu, Y. Song, W. Lv, Z. Duan, et al., Mechanistic understanding of the electrocatalytic conversion of CO into C2+ products by double-atom catalysts, Mater. Today Phys. 37 (2023) 101203.
[56] K. Zhao, X. Nie, H. Wang, S. Chen, X. Quan, H. Yu, et al., Selective electroreduction of CO2 to acetone by single copper atoms anchored on N-doped porous carbon, Nat. Commun. 11 (1) (2020) 2455.